

First-principles scattering-state approach for nonlinear electrical transport in nanostructures

Hyoung Joon Choi,^{1,2,*} Marvin L. Cohen,^{2,3} and Steven G. Louie^{2,3}

¹*Department of Physics and IPAP, Yonsei University, Seoul 120-749, Korea*

²*Department of Physics, University of California, Berkeley, California 94720, USA*

³*Materials Sciences Division, Lawrence Berkeley National Laboratory, Berkeley, California 94720, USA*

(Received 30 December 2006; revised manuscript received 26 August 2007; published 19 October 2007)

We present an *ab initio* scattering-state method for calculating the electrical transport properties of nanostructures at a finite bias voltage. A typical system of interest consists of two semi-infinite crystalline metal probes and a nanostructure (e.g., an atomic wire or a molecule) placed between the probes. The two metal probes have different chemical potentials at a finite bias voltage. The electronic structure of the system is described by the Kohn-Sham density functional method, with appropriate boundary conditions imposed on the electronic density and potential inside the metal probes. We expand the electronic wave functions with pseudoatomic orbitals and directly solve the self-consistent Kohn-Sham equation to obtain the transmission probabilities of electrons incident from either of the probes. The current through the molecule or nanostructure is then obtained by integrating the transmission between the two chemical potentials. Our scattering-state method provides stable and efficient algorithms for the complex bands, scattering-state wave functions, and the nonequilibrium steady-state electron density. As illustrations of the method, we present the calculated electrical transport properties of a defective carbon nanotube, a four-carbon atomic chain, and a benzene-dithiol molecular junction.

DOI: [10.1103/PhysRevB.76.155420](https://doi.org/10.1103/PhysRevB.76.155420)

PACS number(s): 73.63.-b, 73.22.-f, 85.65.+h

I. INTRODUCTION

Nanometer-scale electronic conduction has been measured in various systems including atomic point contacts,^{1,2} atomic wires,^{3–5} and molecular electronic devices.^{6–12} In such nanometer-scale systems, the electronic conduction is determined by the quantum-mechanical states of electrons,^{13–17} and the conduction is highly dependent on the detailed atomic configurations of the systems. Based on first-principles electronic structure calculations,^{18–22} computational methods have been developed for more realistic simulations of the electronic conduction.^{23–34,36–38} In these methods, nanometer-scale systems are regarded as collections of valence electrons and ions, and the electrons are described as quantum-mechanical waves.

Simulations of electronic conduction have two important components that are not considered in standard electronic structure calculations. First, the electrical current is carried by scattering states of electrons satisfying different boundary conditions from those considered in solids or clusters. Second, especially in the case of a finite bias voltage, the systems under consideration have at least two chemical potentials which differ by the applied bias voltage. These two components pose two of the major challenges for calculating the electronic conduction.

When an applied bias voltage is small enough, the electron distribution does not significantly differ from the equilibrium distribution at zero bias voltage. In such situations, the (linear-response) conductance may be determined by the transmission coefficients of the scattering states or from the Green's functions.^{13–17} The linear-response conductance has been studied for various systems. For example, atomic wires between metal electrodes have been studied using a jellium model for the electrodes,^{23–25} and silicon atomic wires have been studied using a local pseudopotential to model the sili-

con atoms.²⁶ Defective carbon nanotubes have been studied using *ab initio* nonlocal pseudopotentials^{19,20} for the constituent atoms and plane waves for the expansion of the scattering-state wave functions.^{27,28} Linear-response calculations have also been performed with pseudoatomic basis sets,^{29–31} real-space grids,³² and Wannier functions.³³ In calculating the linear-response conductance, the main component is a stable and efficient algorithm for the calculation of transmission coefficients or their equivalents.

In nanometer-scale systems, the current-voltage characteristics often show a nonlinear behavior as the applied bias voltage grows. To understand the conduction mechanisms in individual systems, the electron distribution should be calculated self-consistently at a finite bias voltage, and so should the transmission coefficients or their equivalents. The most important step in the calculation is obtaining the electron distribution by integrating scattering-state wave functions, or nonequilibrium Green's functions (NEGFs), between two or more chemical potentials. NEGF methods have been developed and applied to nonlinear electrical properties of various systems.^{34–37} The jellium-model method for metal electrodes was also developed to examine the nonlinear electrical behavior of molecules sandwiched between two metal electrodes.³⁸

In this paper, we present an *ab initio* scattering-state method for nonlinear electrical properties of nanometer-scale systems at a finite bias voltage. In our method, we calculate the transmission spectra and the electron density from scattering-state wave functions. A major advance in our method is the achievement of stable and accurate algorithms for scattering-state wave functions and their integration for the electron density at a finite bias voltage. Our method can be implemented straightforwardly to any localized-orbital-based computer program for electronic structure calculations. In the present work, the SIESTA code²² is used as a host program for encoding our method.

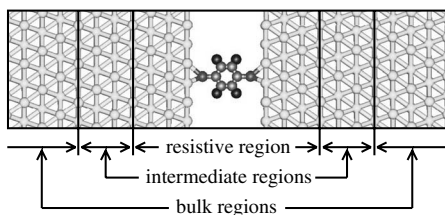


FIG. 1. Two-probe setup for conductance measurement of a nanostructure. As an example, a benzene-dithiol molecule is shown, placed between two gold (111) surfaces.

This paper is organized as follows. In Sec. II, we present our scattering-state method for nonlinear electrical transport at a finite bias voltage. Then, in Sec. III, we apply our method to a carbon nanotube with a pentagon-heptagon-pair defect, a four-carbon atomic chain placed between aluminum bars, and a benzene-dithiol ($C_6H_4S_2$) molecule contacted with two Au (111) surfaces, and compare our results with those in the literature. Finally, we summarize our study in Sec. IV.

II. SCATTERING-STATE APPROACH FOR NONLINEAR ELECTRICAL TRANSPORT

A. Overview

Figure 1 shows a prototype of nanometer-scale systems which we consider in the present study. It is a two-probe measurement setup in which a nanometer-scale sample is placed between two metal probes. Using the atomic structures of the sample and the metal probes, we describe the electronic structure of the system with *ab initio* pseudopotentials^{18,19} and the Kohn-Sham density functional theory (DFT). The system under consideration is an open system, and the chemical potentials of the two metal probes are different at a finite bias voltage. Proper boundary conditions are needed for the Hartree potential, the Kohn-Sham Hamiltonian, and the electronic wave functions. The electron density is determined self-consistently at a finite bias voltage using scattering states which satisfy the self-consistent Kohn-Sham equation with scattering boundary conditions. Once self-consistency is reached, the current through the sample is determined from the transmission coefficients which are obtained from the scattering-state wave functions.

The present formalism provides a stable and accurate calculational approach for the complex band structure, scattering states, and the nonequilibrium electron density at steady state. This section is organized as follows. The atomic structure of the prototype system is described in Sec. II B. The theoretical framework for calculating the electron density and the Hartree potential in a two-probe setup is presented in Sec. II C. The Kohn-Sham effective potential is discussed in Sec. II D. The matrix representation of the Hamiltonian is derived in Sec. II E. A method for the complex band structure in a probe is presented in detail in Sec. II F. Computational methods for scattering-state wave functions, the nonequilibrium electron density, and the current are provided in Secs. II G–II I, respectively.

B. Atomic structure of a conductance measurement setup

We consider a two-probe measurement setup for a nanometer-scale sample, as shown in Fig. 1. An atomic wire or a molecule is placed between two crystalline metal probes, and the probes are assumed to be semi-infinite in length in either direction. With this setup, we consider the current through the sample when a finite bias voltage is applied between the probes. The bias voltage is represented by the difference of the two chemical potentials of the probes. The nonlinear electrical conduction is determined by calculating the electronic structure and the current in the system self-consistently at each finite bias voltage. Although a two-probe setup is assumed in this study, our method is applicable to multiprobe cases in general.

We divide the two-probe setup into five regions in the theoretical description: a resistive region, two intermediate regions, and two semi-infinite bulk regions. The resistive region contains the nanometer-scale sample itself and parts of the probes connected to it. The resistive region should contain large enough parts of the probes so that the voltage drop occurs inside the region and is negligible outside. In the Intermediate and bulk regions, the metal probes are assumed to have perfect crystal structures with periodic atomic configurations of certain unit cell length. The intermediate regions are the first unit cell of the metal probes just outside the resistive region. We distinguish these from the other unit cells of the probes for clarity. In the case that we need an intermediate region which is greater than a primitive unit cell, a description is given in Sec. II D. We make the intermediate region consist of several primitive unit cells and define it as a unit cell of the corresponding probe. In the bulk regions of the two-probe setup, we assume that the electronic structures of the bulk metals are not perturbed by the presence of the resistive region. In addition, we assume that the atomic structure of the whole setup is periodic in x and y directions, which are parallel to the metal surfaces in a supercell arrangement.

C. Electron distribution and Hartree potential

In the two-probe setup, the electron distribution is calculated separately in the resistive region and in the intermediate and bulk regions. In the resistive region, the electron distribution is obtained from the scattering-state wave functions, as described in Sec. II H. In the intermediate and bulk regions, the electron distribution is assumed to be the same as that in the corresponding bulk metals. We obtain the bulk electron distribution by separate self-consistent electronic structure calculations, in each of which we consider only one unit cell and apply periodic boundary conditions to simulate a truly bulk system as in standard calculations. The obtained bulk electron distribution is used for the intermediate and bulk regions, and then the exchange-correlation potential is calculated for those regions.

The Hartree potential is also calculated separately in the resistive region and in the intermediate and bulk regions. Then, it is matched continuously on the boundary planes between the regions. In the intermediate and bulk regions, the Hartree potential is assumed to be the same as in the

corresponding bulk metals except for a possible constant shift due to the applied bias voltage. This assumption is valid if the resistive region contains large enough parts of the probes so that the potential outside the resistive region is perturbed negligibly by the presence of the surfaces of the probes, the nanometer-scale sample, and the voltage drop. Thus, the Hartree potentials of the bulk metals are saved in the same separate self-consistent calculation that we used to calculate the bulk electron distributions, and then they are used for the potential in the corresponding intermediate and bulk regions of the two-probe setup. The bulk Hartree potential is uniformly shifted inside the intermediate and bulk regions relative to that in the similar regions across the sample in the case that a finite bias voltage is applied between the probes. We use also the Hartree potentials of the bulk metals even on the boundary planes between the resistive region and the intermediate regions, so the values of the potential on the boundary planes fix the boundary conditions for the potential inside the resistive region.

In the resistive region, the Hartree potential is determined by the Poisson equation inside the region and the values on the boundary planes between the resistive and the intermediate regions. The boundary values are determined by the potential in the intermediate regions, which is obtained from separate bulk calculations, as mentioned above. Since the Poisson equation and the boundary conditions determine the Hartree potential inside the resistive region uniquely, no degree of freedom is left to make the normal derivative of the potential continuous on the boundary planes. Thus, the normal derivative of the Hartree potential may not be exactly continuous on the boundary planes, but the discontinuity will be negligible if the resistive region is large enough to contain most of the screening charges in the probes near the nanometer-scale sample.

The Poisson equation in the resistive region is solved in momentum space. First, the charge density in the resistive region is mapped to a real-space grid in a supercell which is larger than the original resistive region. Since charge accumulation may happen in the nanostructure due to the induced current, the resistive region may have nonzero net charge. Thus, to neutralize the charge distribution in the supercell before the Fourier transformation without changing the Poisson equation inside the resistive region, we introduce a compensating charge inside the supercell but outside the resistive region.³⁹ The charge distribution in the supercell is then Fourier transformed to momentum space, where the Hartree potential is calculated. After the potential is Fourier transformed back to the real-space grid in the supercell, we take the values of the potential only inside the resistive region and on its boundary planes. Finally, we add a general solution of the Laplace equation to the potential inside the resistive region and on the boundary planes so that the values of the Hartree potential on the boundary planes are equal to the corresponding bulk values of the probes. In the case of a rectangular resistive region, the added general solution is a linear combination of simple sinusoidal and exponential functions with coefficients that satisfy the boundary conditions. This procedure produces the Hartree potential in the resistive region, which will be used in the Kohn-Sham equation.

D. Kohn-Sham effective potential and Hamiltonian matrix

In this subsection, we consider the Hamiltonian matrix representing the Kohn-Sham effective potential in the two-probe setup. We assume that DFT within the local density approximation or the generalized gradient approximation is still valid for the nanometer-scale sample and the probes even at a finite bias voltage. *Ab initio* norm-conserving pseudopotentials are used to describe electron-ion interactions, and the Hamiltonian matrix elements are evaluated with respect to localized pseudoatomic orbitals.²²

The Kohn-Sham effective potential is determined by the exchange-correlation potential (via the electron distribution), the Hartree potential, and the ionic pseudopotentials. As described in Sec. II B, the two-probe setup shown in Fig. 1 consists of five regions: a resistive region, two intermediate regions, and two semi-infinite bulk regions. As mentioned in Sec. II C, the resistive region is assumed to be so large that it leaves a negligible voltage drop in the intermediate and bulk regions. Thus, one can perform separate electronic structure calculations of bulk metals and substitute the obtained electron distributions and Hartree potentials for those in the intermediate and bulk regions. After this substitution and the calculation of corresponding potentials in the resistive region, one can evaluate Hamiltonian matrix elements in the two-probe setup with respect to the basis functions. In the case of the bulk regions, apart from a constant due to the bias voltage, the matrix elements should be the same as those obtained from the separate bulk-metal calculations, so one can use the results of the bulk-metal calculations. In the case of the intermediate regions, it should be noted that although the Kohn-Sham effective potential is the same as its bulk value, the associated Hamiltonian matrix elements may differ from their bulk ones because some of the localized orbitals of atoms in the intermediate regions overlap orbitals in the resistive region, where the potential may deviate from that of a bulk metal.

To have the exact same Kohn-Sham effective potential in the intermediate regions as in the bulk regions, as assumed above, the following constraint should be imposed on the atomic structure in the resistive region. If an atom in the resistive region has a neutral-atomic potential overlapping with one of the intermediate regions, the position of the atom, when translated by one unit cell length toward the intermediate region, should coincide with the position of one of the atoms there. A sufficient condition for this constraint is to make the resistive region large enough to have at least one bulk unit cell at the interface.

For technical reasons of making the method stable and efficient, we impose additional conditions on the sizes of the resistive region and the intermediate regions to make the Hamiltonian matrix elements satisfy certain mathematical conditions. When we decide the size of the resistive region, we make the resistive region large enough so that all the matrix elements are zero between any orbital in one intermediate region and any other orbital in the other intermediate region. In other words, there is no direct coupling between the two intermediate regions. We also impose similar conditions on the sizes of the intermediate regions. An intermediate region should be large enough to prevent any nonzero

matrix element between the resistive region and the corresponding semi-infinite bulk region. If the size of an intermediate region needs to be increased to satisfy this condition, we make it contain several primitive unit cells and then define the intermediate region as a new unit cell of the corresponding semi-infinite bulk region, as mentioned in Sec. II B. The above conditions on the sizes of the regions will be used in deriving the Hamiltonian equation in Sec. II E.

Since the semi-infinite bulk regions are assumed to have perfect crystal structures and unperturbed electronic structures, the matrix elements of the Kohn-Sham equation in a bulk region appear periodically along the probe. Thus, only a *finite* number of distinct matrix elements are needed to produce the infinite-dimensional Hamiltonian matrix equation in the two-probe setup, even though the system is infinite and has no periodic boundary condition as a whole.

E. Hamiltonian equation in the two-probe setup

In this subsection, we derive a matrix representation of the Kohn-Sham Hamiltonian equation,

$$(\hat{H} - E)|\psi\rangle = 0, \quad (1)$$

in the two-probe setup. Here, \hat{H} is the Kohn-Sham Hamiltonian operator and $|\psi\rangle$ is the electronic state of energy E . Since the two-probe setup is an infinite system with no periodic boundary conditions, the energy E forms a continuous spectrum. The only well-defined quantum number in the system except for E , in general, is the parallel wave vector \mathbf{k}_{\parallel} , which is associated with the supercell periodic boundary conditions in the x and y directions that are parallel to the metal surfaces. In the present work, we use localized orbitals to expand the electronic wave function $|\psi\rangle$ and obtain a matrix equation representing Eq. (1).

In a localized-orbital expansion, the electronic wave function $|\psi\rangle$ is given in the form

$$|\psi\rangle = \sum_{\mathbf{R}_{\parallel}} e^{i\mathbf{k}_{\parallel} \cdot \mathbf{R}_{\parallel}} \left[\sum_{i=1}^{N_0} C_{i,\mathbf{k}_{\parallel}}^{(0)} |i; \mathbf{R}_{\parallel}\rangle + \sum_{u=1}^{\infty} \sum_{l=1}^{N_l} C_{iu,\mathbf{k}_{\parallel}}^{(1)} |i, u, 1; \mathbf{R}_{\parallel}\rangle + \sum_{u=1}^{\infty} \sum_{l=1}^{N_l} C_{iu,\mathbf{k}_{\parallel}}^{(2)} |i, u, 2; \mathbf{R}_{\parallel}\rangle \right], \quad (2)$$

where \mathbf{R}_{\parallel} indicates a supercell in the x and y directions (which are parallel to the metal surfaces), $|i; \mathbf{R}_{\parallel}\rangle$ is the i th orbital of the resistive region in the supercell at \mathbf{R}_{\parallel} , $|i, u, l; \mathbf{R}_{\parallel}\rangle$ is the i th orbital of the u th unit cell of the l th probe. In the expansion, N_0 is the number of orbitals of the resistive region and N_l is the number of orbitals of a unit cell of the l th probe. The coefficients $C_{i,\mathbf{k}_{\parallel}}^{(0)}$ and $C_{iu,\mathbf{k}_{\parallel}}^{(l)}$ are complex numbers, in general.

Now, we derive a matrix representation of Eq. (1) in the resistive, intermediate, and bulk regions. First, we project Eq. (1) onto the i th orbital of the resistive region in the supercell at the origin (which we denote with $\mathbf{0}$) and have

$$\sum_{\mathbf{R}_{\parallel}} e^{i\mathbf{k}_{\parallel} \cdot \mathbf{R}_{\parallel}} \left[\sum_{j=1}^{N_0} \langle i; \mathbf{0} | \hat{H} - E | j; \mathbf{R}_{\parallel} \rangle C_{j,\mathbf{k}_{\parallel}}^{(0)} + \sum_{j=1}^{N_1} \langle i; \mathbf{0} | \hat{H} - E | j, 1, 1; \mathbf{R}_{\parallel} \rangle C_{j1,\mathbf{k}_{\parallel}}^{(1)} + \sum_{j=1}^{N_2} \langle i; \mathbf{0} | \hat{H} - E | j, 1, 2; \mathbf{R}_{\parallel} \rangle C_{j1,\mathbf{k}_{\parallel}}^{(2)} \right] = 0. \quad (3)$$

Here, we have used the condition that the intermediate regions are so thick that no orbital in the resistive region interacts directly with any orbital in the bulk regions of the probes. Next, we consider the projection of Eq. (1) onto an orbital in the intermediate regions, which we define as the first unit cells of the crystalline probes. When Eq. (1) is projected onto $|i, 1, l; \mathbf{0}\rangle$, which is the i th orbital of the first unit cell of the l th probe in the supercell at the origin, the equation becomes

$$\sum_{\mathbf{R}_{\parallel}} e^{i\mathbf{k}_{\parallel} \cdot \mathbf{R}_{\parallel}} \left[\sum_{j=1}^{N_0} \langle i, 1, l; \mathbf{0} | \hat{H} - E | j; \mathbf{R}_{\parallel} \rangle C_{j,\mathbf{k}_{\parallel}}^{(0)} + \sum_{j=1}^{N_l} \langle i, 1, l; \mathbf{0} | \hat{H} - E | j, 1, l; \mathbf{R}_{\parallel} \rangle C_{j1,\mathbf{k}_{\parallel}}^{(l)} + \sum_{j=1}^{N_l} \langle i, 1, l; \mathbf{0} | \hat{H} - E | j, 2, l; \mathbf{R}_{\parallel} \rangle C_{j2,\mathbf{k}_{\parallel}}^{(l)} \right] = 0. \quad (4)$$

Here, we have used the condition that the resistive region is so thick that no orbital of an intermediate region interacts directly with any orbital of the other intermediate region. In addition, we assume that the unit cell in the probe is so thick that only orbitals between neighboring unit cells have non-zero matrix elements. Finally, we consider orbitals in the bulk regions of the probes. We project Eq. (1) onto the i th orbital of the u th unit cell ($u \geq 2$) of the l th probe and have

$$\sum_{\mathbf{R}_{\parallel}} e^{i\mathbf{k}_{\parallel} \cdot \mathbf{R}_{\parallel}} \left[\sum_{j=1}^{N_l} \langle i, 2, l; \mathbf{0} | \hat{H} - E | j, 1, l; \mathbf{R}_{\parallel} \rangle C_{j(u-1),\mathbf{k}_{\parallel}}^{(l)} + \sum_{j=1}^{N_l} \langle i, 2, l; \mathbf{0} | \hat{H} - E | j, 2, l; \mathbf{R}_{\parallel} \rangle C_{ju,\mathbf{k}_{\parallel}}^{(l)} + \sum_{j=1}^{N_l} \langle i, 1, l; \mathbf{0} | \hat{H} - E | j, 2, l; \mathbf{R}_{\parallel} \rangle C_{j(u+1),\mathbf{k}_{\parallel}}^{(l)} \right] = 0. \quad (5)$$

Here, we have used the assumption that the matrix elements in the bulk regions are invariant under translation by one unit cell length as defined above. In order to write the equations in more compact forms, we define matrices as follows. We define

$$\mathcal{H}_{ij,\mathbf{k}_{\parallel}}^{(00)} = \sum_{\mathbf{R}_{\parallel}} e^{i\mathbf{k}_{\parallel} \cdot \mathbf{R}_{\parallel}} \langle i; \mathbf{0} | \hat{H} - E | j; \mathbf{R}_{\parallel} \rangle \quad (6a)$$

for the i th and j th orbitals of the resistive region,

$$\mathcal{H}_{ij,\mathbf{k}_{\parallel}}^{(0l)} = \sum_{\mathbf{R}_{\parallel}} e^{i\mathbf{k}_{\parallel} \cdot \mathbf{R}_{\parallel}} \langle i; \mathbf{0} | \hat{H} - E | j, 1, l; \mathbf{R}_{\parallel} \rangle \quad (6b)$$

for the i th orbital of the resistive region and the j th orbital of the intermediate region (the first unit cell) of the l th probe ($l=1$ or 2),

$$\mathcal{H}_{ij,\mathbf{k}_{\parallel}}^{(l0)} = \sum_{\mathbf{R}_{\parallel}} e^{i\mathbf{k}_{\parallel} \cdot \mathbf{R}_{\parallel}} \langle i, 1, l; \mathbf{0} | \hat{H} - E | j; \mathbf{R}_{\parallel} \rangle \quad (6c)$$

for the i th orbital of the intermediate region of the l th probe and the j th orbital of the resistive region, and

$$\mathcal{H}_{ij,\mathbf{k}_{\parallel}}^{(ll)} = \sum_{\mathbf{R}_{\parallel}} e^{i\mathbf{k}_{\parallel} \cdot \mathbf{R}_{\parallel}} \langle i, 1, l; \mathbf{0} | \hat{H} - E | j, 1, l; \mathbf{R}_{\parallel} \rangle \quad (6d)$$

for the i th and j th orbitals of the intermediate region of the l th probe. For orbitals in the bulk regions of the l th probe, we define

$$\mathcal{H}_{ij,\mathbf{k}_{\parallel}}^{(l-)} = \sum_{\mathbf{R}_{\parallel}} e^{i\mathbf{k}_{\parallel} \cdot \mathbf{R}_{\parallel}} \langle i, u, l; \mathbf{0} | \hat{H} - E | j, u-1, l; \mathbf{R}_{\parallel} \rangle, \quad (7a)$$

$$\mathcal{H}_{ij,\mathbf{k}_{\parallel}}^{(l)} = \sum_{\mathbf{R}_{\parallel}} e^{i\mathbf{k}_{\parallel} \cdot \mathbf{R}_{\parallel}} \langle i, u, l; \mathbf{0} | \hat{H} - E | j, u, l; \mathbf{R}_{\parallel} \rangle, \quad (7b)$$

$$\mathcal{H}_{ij,\mathbf{k}_{\parallel}}^{(l+)} = \sum_{\mathbf{R}_{\parallel}} e^{i\mathbf{k}_{\parallel} \cdot \mathbf{R}_{\parallel}} \langle i, u-1, l; \mathbf{0} | \hat{H} - E | j, u, l; \mathbf{R}_{\parallel} \rangle, \quad (7c)$$

where $u=2, 3, \dots, \infty$ but the matrices are independent of the unit cell index u . All these matrices have complex-valued elements, in general. Using these matrices, we obtain the following matrix representations of the Hamiltonian equation:

$$\sum_{j=1}^{N_0} \mathcal{H}_{ij}^{(00)} C_j^{(0)} + \sum_{j=1}^{N_1} \mathcal{H}_{ij}^{(01)} C_{j1}^{(1)} + \sum_{j=1}^{N_2} \mathcal{H}_{ij}^{(02)} C_{j1}^{(2)} = 0 \quad (8a)$$

for the i th orbital of the resistive region,

$$\sum_{j=1}^{N_0} \mathcal{H}_{ij}^{(l0)} C_j^{(0)} + \sum_{j=1}^{N_l} \mathcal{H}_{ij}^{(ll)} C_{j1}^{(l)} + \sum_{j=1}^{N_l} \mathcal{H}_{ij}^{(l+)} C_{j2}^{(l)} = 0 \quad (8b)$$

for the i th orbital of the intermediate region of the l th probe ($l=1$ or 2), and

$$\sum_{j=1}^{N_l} \mathcal{H}_{ij}^{(l-)} C_{j(u-1)}^{(l)} + \sum_{j=1}^{N_l} \mathcal{H}_{ij}^{(l)} C_{ju}^{(l)} + \sum_{j=1}^{N_l} \mathcal{H}_{ij}^{(l+)} C_{j(u+1)}^{(l)} = 0 \quad (8c)$$

for the i th orbital of the bulk region ($u=2, 3, \dots, \infty$) of the l th probe. The parallel wave vector \mathbf{k}_{\parallel} is omitted for simplicity. We will first search for complex-band solutions of Eq. (8c) in Sec. II F and then scattering-state solutions of Eqs. (8a)–(8c) in Sec. II G.

F. Complex band structure in each probe

In this subsection, we consider a general solution of Eq. (8c), which is

$$\sum_{j=1}^N \mathcal{H}_{ij}^- C_{j(u-1)} + \sum_{j=1}^N \mathcal{H}_{ij} C_{ju} + \sum_{j=1}^N \mathcal{H}_{ij}^+ C_{j(u+1)} = 0 \quad (9)$$

for $u=2, 3, \dots, \infty$. In the above equation, we have omitted the index l for a probe for simplicity. This matrix equation is effectively a recurrence relation which determines $C_{j(u+1)}$ from $C_{j(u-1)}$ and C_{ju} . If the matrix \mathcal{H}_{ij}^+ is far from a singular matrix, it is straightforward to obtain the recurrence relation using the inverse of the matrix \mathcal{H}_{ij}^+ .^{40,41} In general, however, the matrix \mathcal{H}_{ij}^+ is often a singular matrix or very close to it.⁴¹

In order to isolate any singularity in \mathcal{H}_{ij}^+ , we first obtain a singular-value-decomposed form of the matrix \mathcal{H}_{ij}^+ .^{41,42}

$$\mathcal{H}_{ij}^+ = \sum_{s=1}^N h_s U_{is} V_{js}^*, \quad (10)$$

where the asterisk represents a complex conjugate. Here, h_i 's are non-negative real numbers arranged in descending order, and U_{ij} and V_{ij} are unitary matrices, that is,

$$\sum_{s=1}^N U_{si}^* U_{sj} = \delta_{ij}, \quad \sum_{s=1}^N V_{si}^* V_{sj} = \delta_{ij}. \quad (11)$$

Numerical libraries such as LAPACK provide routines for the singular-value decomposition. We can use Eq. (10) to obtain a singular-value-decomposed form of \mathcal{H}_{ij}^- since \mathcal{H}_{ij}^- is the Hermitian conjugate of \mathcal{H}_{ij}^+ . Thus, we have

$$\mathcal{H}_{ij}^- = \sum_{s=1}^N h_s V_{is} U_{js}^*. \quad (12)$$

Substituting Eqs. (10) and (12) to Eq. (9) and using $\sum_{t=1}^N V_{st} V_{jt}^* = \delta_{sj}$, we have

$$\begin{aligned} & \sum_{j=1}^N \sum_{s=1}^N h_s V_{is} U_{js}^* C_{j(u-1)} + \sum_{j=1}^N \sum_{s=1}^N \sum_{t=1}^N \mathcal{H}_{is} V_{st} V_{jt}^* C_{ju} \\ & + \sum_{j=1}^N \sum_{s=1}^N h_s U_{is} V_{js}^* C_{j(u+1)} = 0. \end{aligned} \quad (13)$$

Using unitary transformations represented by the matrices U_{ij} and V_{ij} , we define coefficients X_{iu} and Y_{iu} , respectively, as

$$X_{iu} = \sum_{j=1}^N V_{ji}^* C_{ju}, \quad (14a)$$

$$Y_{iu} = \sum_{j=1}^N U_{ji}^* C_{j(u-1)} \quad (14b)$$

for $u=2, 3, \dots, \infty$. We also define two matrices M_{ij} and O_{ij} as

$$M_{ij} = \sum_{s=1}^N \sum_{t=1}^N V_{si}^* \mathcal{H}_{st} V_{tj}, \quad (15a)$$

$$O_{ij} = \sum_{s=1}^N U_{si}^* V_{sj}. \quad (15b)$$

With the coefficients X_{iu} and Y_{iu} defined by Eqs. (14a) and (14b), becomes

$$\sum_{s=1}^N h_s V_{is} Y_{su} + \sum_{j=1}^N \mathcal{H}_{ij} \sum_{s=1}^N V_{js} X_{su} + \sum_{s=1}^N h_s U_{is} X_{s(u+1)} = 0. \quad (16)$$

We transform the equation with V_{ij}^* ,

$$\sum_{i=1}^N V_{it}^* \left[\sum_{s=1}^N h_s V_{is} Y_{su} + \sum_{j=1}^N \mathcal{H}_{ij} \sum_{s=1}^N V_{js} X_{su} + \sum_{s=1}^N h_s U_{is} X_{s(u+1)} \right] = 0, \quad (17)$$

which reduces to a form

$$h_i Y_{iu} + \sum_{j=1}^N M_{ij} X_{ju} + \sum_{j=1}^N O_{ji}^* h_j X_{j(u+1)} = 0, \quad (18)$$

where we used the matrices M_{ij} and O_{ij} defined by Eqs. (15a) and (15b). In order to use this equation as a recurrent relation between $\{X_{i(u+1)}, Y_{i(u+1)}\}$ and $\{X_{iu}, Y_{iu}\}$, we need another equation which can produce $Y_{i(u+1)}$ from X_{iu} and Y_{iu} . We obtain the required equation by combining the inverse of Eq. (14a),

$$C_{iu} = \sum_{j=1}^N V_{ij} X_{ju}, \quad (19)$$

with Eq. (14b) for $Y_{i(u+1)}$, that is,

$$Y_{i(u+1)} = \sum_{s=1}^N U_{si}^* \sum_{j=1}^N V_{sj} X_{ju} = \sum_{j=1}^N O_{ij} X_{ju}, \quad (20)$$

which is valid for $u \geq 2$. Now, Eqs. (18) and (20) provide a recurrence relation which determines $X_{i(u+1)}$ and $Y_{i(u+1)}$ from X_{iu} and Y_{iu} for $u \geq 2$.

When \mathcal{H}_{ij}^+ is a singular matrix or close to it, some of h_i are zero or very close to zero. Suppose that h_i for $i > n$ are less than a certain small number, h_{cur} , so that they are regarded as zero. Then, we can split Eq. (18) into two sets:

$$h_i Y_{iu} + \sum_{j=1}^N M_{ij} X_{ju} + \sum_{j=1}^n O_{ji}^* h_j X_{j(u+1)} = 0 \quad (21)$$

for $i \leq n$ and

$$\sum_{j=1}^N M_{ij} X_{ju} + \sum_{j=1}^n O_{ji}^* h_j X_{j(u+1)} = 0 \quad (22)$$

for $i > n$. We will use Eq. (22) to eliminate the coefficients X_{iu} for $i > n$ in Eqs. (21) and (20). We rearrange the terms in Eq. (22) and have

$$\sum_{j=n+1}^N M_{ij} X_{ju} = - \sum_{j=1}^n M_{ij} X_{ju} - \sum_{j=1}^n O_{ji}^* h_j X_{j(u+1)} \quad (23)$$

for $i > n$. If the submatrix M_{ij} on the left-hand side is not singular, Eq. (23) determines X_{iu} for $i > n$ from X_{iu} and $X_{i(u+1)}$ for $i \leq n$. The submatrix M_{ij} on the left-hand side in Eq. (23) is very unlikely to be a singular matrix because it is a diagonal sub-block (for $i, j > n$) of the (unitary-transformed) Hamiltonian matrix. We thus obtain a relation,

$$X_{iu} = \sum_{j=1}^n \alpha_{ij} X_{ju} + \sum_{j=1}^n \beta_{ij} X_{j(u+1)} \quad (24)$$

for $i > n$, where the matrices α_{ij} and β_{ij} are determined by solving

$$\sum_{s=n+1}^N M_{is} \alpha_{sj} = -M_{ij}, \quad (25a)$$

$$\sum_{s=n+1}^N M_{is} \beta_{sj} = -O_{ji}^* h_j \quad (25b)$$

for $n < i \leq N$ and $1 \leq j \leq n$.

Substituting Eq. (24) for X_{iu} (for $i > n$) in Eqs. (20) and (21) and rearranging terms, we obtain

$$\begin{aligned} \sum_{j=1}^n \left(M_{ij} + \sum_{s=n+1}^N M_{is} \alpha_{sj} \right) X_{ju} + h_i Y_{iu} \\ = - \sum_{j=1}^n \left(O_{ji}^* h_j + \sum_{s=n+1}^N M_{is} \beta_{sj} \right) X_{j(u+1)}, \end{aligned} \quad (26a)$$

$$\sum_{j=1}^n \left(O_{ij} + \sum_{s=n+1}^N O_{is} \alpha_{sj} \right) X_{ju} = - \sum_{j=1}^n \sum_{s=n+1}^N O_{is} \beta_{sj} X_{j(u+1)} + Y_{i(u+1)} \quad (26b)$$

for $i \leq n$ and $u \geq 2$. This system of equations is effectively a recurrence relation (valid even for a singular \mathcal{H}_{ij}^+), which determines $X_{i(u+1)}$ and $Y_{i(u+1)}$ from X_{iu} and Y_{iu} for $i \leq n$ and $u \geq 2$. Once X_{i2} and Y_{i2} for $i \leq n$ are given, we can apply Eqs. (26a) and (26b) repeatedly and determine X_{iu} and Y_{iu} for all $i \leq n$ and $u \geq 3$. Then, we use Eq. (24) to obtain X_{iu} for $n < i \leq N$ and $u \geq 2$, and Eq. (20) to obtain Y_{iu} for $n < i \leq N$ and $u \geq 3$. Therefore, the coefficients X_{i2} and Y_{i2} for $i \leq n$ determine all X_{iu} and Y_{iu} for $u \geq 2$, except for Y_{i2} for $n < i \leq N$. This means that a general solution satisfying Eq. (9) for all $u \geq 2$ has only $n+N$ remaining independent coefficients (in other words, the solution has $n+N$ degrees of freedom) when the singularity of the matrix \mathcal{H}_{ij}^+ is regarded $(N-n)$ -fold.

Now, we search for “periodic” solutions of Eqs. (26a) and (26b) in the sense that X_{iu} and Y_{iu} are given as

$$X_{iu} = (e^{ika})^{u-2} P_i(k), \quad (27a)$$

$$Y_{iu} = (e^{ika})^{u-2} Q_i(k) \quad (27b)$$

for $i \leq n$ and $u \geq 2$. Here, a is a unit cell length in a probe under consideration and k is a complex number in general.

By substituting Eqs. (27a) and (27b) into Eqs. (26a) and (26b), we obtain equations for $P_i(k)$ and $Q_i(k)$:

$$\sum_{j=1}^n \left(M_{ij} + \sum_{s=n+1}^N M_{is} \alpha_{sj} \right) P_j(k) + h_i Q_i(k) = -e^{ika} \sum_{j=1}^n \left(O_{ji}^* h_j + \sum_{s=n+1}^N M_{is} \beta_{sj} \right) P_j(k), \quad (28a)$$

$$\sum_{j=1}^n \left(O_{ij} + \sum_{s=n+1}^N O_{is} \alpha_{sj} \right) P_j(k) = -e^{ika} \left(\sum_{j=1}^n \sum_{s=n+1}^N O_{is} \beta_{sj} P_j(k) + Q_i(k) \right) \quad (28b)$$

for $i \leq n$. It is straightforward to represent Eqs. (28a) and (28b) as generalized eigenvalue equations

$$\sum_{j=1}^{2n} A_{ij} Z_j = \lambda \sum_{j=1}^{2n} B_{ij} Z_j \quad (29)$$

for $i=1, 2, \dots, 2n$. The (general) complex matrices A and B are given by

$$\begin{aligned} A_{ij} &= M_{ij} + \sum_{s=n+1}^N M_{is} \alpha_{sj}, \\ A_{i(j+n)} &= \delta_{ij} h_j, \\ A_{(i+n)j} &= O_{ij} + \sum_{s=n+1}^N O_{is} \alpha_{sj}, \\ A_{(i+n)(j+n)} &= 0, \\ B_{ij} &= -O_{ji}^* h_j - \sum_{s=n+1}^N M_{is} \beta_{sj}, \\ B_{i(j+n)} &= 0, \\ B_{(i+n)j} &= -\sum_{s=n+1}^N O_{is} \beta_{sj}, \\ B_{(i+n)(j+n)} &= \delta_{ij} \end{aligned} \quad (30)$$

for $i, j=1, 2, \dots, n$. We can solve the generalized eigenvalue equation with a numerical library such as LAPACK. If a numerical library is not successful in solving Eq. (29) in practice, it is because some h_i 's in the matrices A and B are still too small to be considered as nonzero numbers. To resolve the problem, we increase h_{cut} and neglect more h_i 's in Eq. (21), transferring some equations from Eq. (21) to Eq. (22). This procedure, when performed repeatedly if needed, decreases the dimensions of the matrices A and B by twice the number of newly discarded h_i 's, and it makes the numerical library work properly. From an obtained eigenvector $Z_j(k)$

corresponding to an eigenvalue $\lambda = e^{ika}$, we retrieve the periodic solution

$$P_j(k) = Z_j(k), \quad Q_j(k) = Z_{j+n}(k)$$

for $j \leq n$. Here, k is a complex number in general. If k is real, the periodic solution represents a propagating electronic wave function. If k is complex with a nonzero imaginary part, the periodic solution represents, in fact, a decaying wave function (or an evanescent wave) in either direction. We define $P_i(k)$ for $i > n$ as

$$P_i(k) = \sum_{j=1}^n (\alpha_{ij} + e^{ika} \beta_{ij}) P_j(k) \quad (32)$$

for simplicity in the following equations.

From Eqs. (2) and (19), the inverse of Eq. (14b), the periodic solutions [$P_i(k)$ and $Q_i(k)$ for $i \leq n$] of Eqs. (26a) and (26b), and $P_i(k)$ for $i > n$ defined by Eq. (32), an electronic wave function of energy E and parallel wave vector \mathbf{k}_{\parallel} in a probe, say, the l th probe, can be generally expressed as

$$|\psi\rangle = \sum_{\mathbf{R}_{\parallel}} e^{i\mathbf{k}_{\parallel} \cdot \mathbf{R}_{\parallel}} \sum_{u=1}^{\infty} \sum_{i=1}^{N_l} C_{iu, \mathbf{k}_{\parallel}}^{(l)} |i, u, l; \mathbf{R}_{\parallel}\rangle, \quad (33)$$

with the coefficients $C_{iu, \mathbf{k}_{\parallel}}^{(l)}$ given by

$$C_{i1, \mathbf{k}_{\parallel}}^{(l)} = \sum_{j=n_l+1}^{N_l} U_{ij, \mathbf{k}_{\parallel}}^{(l)} Y_{j2, \mathbf{k}_{\parallel}}^{(l)} + \sum_k \left(\sum_{j=1}^{n_l} U_{ij, \mathbf{k}_{\parallel}}^{(l)} Q_{j, \mathbf{k}_{\parallel}}^{(l)}(k) \right) C_{\mathbf{k}_{\parallel}}^{(l)}(k), \quad (34a)$$

$$C_{iu, \mathbf{k}_{\parallel}}^{(l)} = \sum_k \left(\sum_{j=1}^{N_l} V_{ij, \mathbf{k}_{\parallel}}^{(l)} P_{j, \mathbf{k}_{\parallel}}^{(l)}(k) \right) C_{\mathbf{k}_{\parallel}}^{(l)}(k) e^{ika(u-2)} \quad (34b)$$

for the unit cell index $u \geq 2$. Here, we have reintroduced the probe index l and the parallel wave vector \mathbf{k}_{\parallel} to emphasize that all the matrices and coefficients are associated with a probe and a parallel wave vector. Expressions (34a) and (34b) have $n_l + N_l$ undetermined coefficients, which are $2n_l$ coefficients of $C_{\mathbf{k}_{\parallel}}^{(l)}(k)$ and $N_l - n_l$ of $Y_{i2, \mathbf{k}_{\parallel}}^{(l)}$ (for $n_l < i \leq N_l$). The coefficients $Y_{j2, \mathbf{k}_{\parallel}}^{(l)}$ for $n_l < i \leq N_l$ appear only in the coefficients $C_{i1, \mathbf{k}_{\parallel}}^{(l)}$ in the first unit cell of the l th probe, and they represent truly localized states inside the intermediate regions.

To summarize, we derived in this subsection a generalized eigenvalue equation [given by Eqs. (29)–(31)] for the complex band structure in a probe, and then a general expression [given by Eqs. (33), (34a), and (34b)] was derived for the electronic wave function of a given energy E in the probe. Possible singularities are well isolated in our method by using a single numerical criterion (h_{cut}) so that our numerical procedure for the complex band structure is stable and robust and highly accurate. In Sec. II G, we will use the general expression for the electronic wave function in a probe to obtain the scattering-state wave functions in the whole system that satisfy Eqs. (8a)–(8c) of Sec. II E.

G. Scattering states in the two-probe setup

In this subsection, we present a method to solve the whole Hamiltonian equation [Eqs. (8a)–(8c)] using the general solutions [Eqs. (34a) and (34b)] obtained in each probe. In particular, we are interested in solutions which represent scattering states of electrons incident from a probe.

The electronic wave function $|\psi\rangle$ in the whole system is given by Eq. (2),

$$|\psi\rangle = \sum_{\mathbf{R}_\parallel} e^{i\mathbf{k}_\parallel \cdot \mathbf{R}_\parallel} \left[\sum_{i=1}^{N_0} C_{i,\mathbf{k}_\parallel}^{(0)} |i; \mathbf{R}_\parallel\rangle + \sum_{u=1}^{\infty} \sum_{i=1}^{N_1} C_{iu,\mathbf{k}_\parallel}^{(1)} |i, u, 1; \mathbf{R}_\parallel\rangle + \sum_{u=1}^{\infty} \sum_{i=1}^{N_2} C_{iu,\mathbf{k}_\parallel}^{(2)} |i, u, 2; \mathbf{R}_\parallel\rangle \right],$$

where \mathbf{R}_\parallel indicates parallel lattice vectors, and $|i; \mathbf{R}_\parallel\rangle$ and $|i, u, l; \mathbf{R}_\parallel\rangle$ are orbitals in the resistive region and in the l th probe, respectively. Their definitions are given below Eq. (2) in Sec. II E. N_0 is the number of orbitals of the resistive region and N_l is the number of orbitals of a unit cell of the l th probe, as defined in Sec. II E.

We suppose that an electron is incident from the first probe. Then, the coefficients $C_{iu}^{(1)}$ for the electronic wave function in the first probe are given by

$$C_{i1}^{(1)} = \sum_{j=1}^{n_1} U_{ij}^{(1)} Q_j^{(1)}(k_0) + \sum_{j=n_1+1}^{N_1} U_{ij}^{(1)} Y_{j2}^{(1)} + \sum_{k \in O_1} \left(\sum_{j=1}^{n_1} U_{ij}^{(1)} Q_j^{(1)}(k) \right) C^{(1)}(k), \quad (35a)$$

$$C_{iu}^{(1)} = \sum_{j=1}^{N_1} V_{ij}^{(1)} P_j^{(1)}(k_0) e^{ik_0 a(u-2)} + \sum_{k \in O_1} \left(\sum_{j=1}^{N_1} V_{ij}^{(1)} P_j^{(1)}(k) \right) C^{(1)}(k) e^{ika(u-2)} \quad (35b)$$

for $1 \leq i \leq N_1$ and $u \geq 2$, where k_0 indicates the wave number of the incident wave and O_1 is the set of the complex bands in the first probe that propagate or decay in the outward direction from the resistive region. Here, the parallel wave vector \mathbf{k}_\parallel is omitted again for brevity. The matrices $U_{ij}^{(1)}$ and $V_{ij}^{(1)}$ are obtained from the singular-value decomposition [Eq. (10)], and n_1 is the number of singular values h_s in the decomposition [Eq. (10)] whose absolute values are greater than a given criterion h_{cut} . The vectors $P_j^{(1)}(k)$ and $Q_j^{(1)}(k)$ are from the eigenvectors of the generalized eigenvalue equation [given by Eqs. (29)–(31)] for the complex band structure. Thus, in the above expression for the coefficients $C_{iu}^{(1)}$, undetermined values are $Y_{j2}^{(1)}$ and $C^{(1)}(k)$. They will be determined by solving the Hamiltonian equation for the whole system. Similarly, the coefficients $C_{iu}^{(2)}$ for the second probe are given by

$$C_{i1}^{(2)} = \sum_{j=n_2+1}^{N_2} U_{ij}^{(2)} Y_{j2}^{(2)} + \sum_{k \in O_2} \left(\sum_{j=1}^{n_2} U_{ij}^{(2)} Q_j^{(2)}(k) \right) C^{(2)}(k), \quad (36a)$$

$$C_{iu}^{(2)} = \sum_{k \in O_2} \left(\sum_{j=1}^{N_2} V_{ij}^{(2)} P_j^{(2)}(k) \right) C^{(2)}(k) e^{ika(u-2)} \quad (36b)$$

for $1 \leq i \leq N_2$ and $u \geq 2$, where O_2 represents the set of *outgoing* complex bands in the second probe. As in the case of the first probe, the matrices $U_{ij}^{(2)}$ and $V_{ij}^{(2)}$ and the number n_2 are determined by the singular-value decomposition [Eq. (10)], and the vectors $P_j^{(2)}(k)$ and $Q_j^{(2)}(k)$ are from the eigenvectors of the generalized eigenvalue equation for the complex band structure. Undetermined values in expressions (36a) and (36b) are $Y_{j2}^{(2)}$ and $C^{(2)}(k)$, which will be determined from the Hamiltonian equation of the whole system, as described below.

The wave function $|\psi\rangle$ of Eq. (2) with the coefficients (35a), (35b), (36a), and (36b) satisfies the Hamiltonian equation [Eq. (8c)] in the probes regardless of the values of undetermined coefficients $C^{(l)}(k)$ and $Y_{j2}^{(l)}$. Thus, remaining non-trivial parts of the Hamiltonian equation are

$$\sum_{j=1}^{N_0} \mathcal{H}_{ij}^{(00)} C_j^{(0)} + \sum_{j=1}^{N_1} \mathcal{H}_{ij}^{(01)} C_{j1}^{(1)} + \sum_{j=1}^{N_2} \mathcal{H}_{ij}^{(02)} C_{j1}^{(2)} = 0 \quad (37a)$$

for the i th orbital ($1 \leq i \leq N_0$) of the resistive region,

$$\sum_{j=1}^{N_0} \mathcal{H}_{ij}^{(10)} C_j^{(0)} + \sum_{j=1}^{N_1} \mathcal{H}_{ij}^{(11)} C_{j1}^{(1)} + \sum_{j=1}^{N_2} \mathcal{H}_{ij}^{(1+)} C_{j2}^{(1)} = 0 \quad (37b)$$

for the i th orbital ($1 \leq i \leq N_1$) of the intermediate region of the first probe, and

$$\sum_{j=1}^{N_0} \mathcal{H}_{ij}^{(20)} C_j^{(0)} + \sum_{j=1}^{N_2} \mathcal{H}_{ij}^{(22)} C_{j1}^{(2)} + \sum_{j=1}^{N_2} \mathcal{H}_{ij}^{(2+)} C_{j2}^{(2)} = 0 \quad (37c)$$

for the i th orbital ($1 \leq i \leq N_2$) of the intermediate region of the second probe. The first equation is Eq. (8a), and the second and third ones are Eq. (8b) with $l=1,2$ substituted explicitly. The number of equations in Eqs. (37a)–(37c) is $N_0 + N_1 + N_2$ ($=N_{tot}$), and it is the same as the number of undetermined coefficients, which is the sum of N_0 for $C_i^{(0)}$, n_1 for $C^{(1)}(k)$ corresponding to outgoing complex bands in the first probe, $N_1 - n_1$ for $Y_{j2}^{(1)}$ (with $i=n_1+1, n_1+2, \dots, N_1$), n_2 for $C^{(2)}(k)$ corresponding to outgoing complex bands in the second probe, and $N_2 - n_2$ for $Y_{j2}^{(2)}$ (with $i=n_2+1, n_2+2, \dots, N_2$). Thus, when Eqs. (35a), (35b), (36a), and (36b) are substituted to Eqs. (37a)–(37c), we obtain a system of inhomogeneous linear algebraic equations

$$\mathcal{A}x = \mathcal{B}, \quad (38)$$

where \mathcal{A} is a $(N_{tot} \times N_{tot})$ -dimensional matrix depending on the electron energy E , x is a N_{tot} -dimensional column vector containing the undetermined coefficients, and \mathcal{B} is a N_{tot} -dimensional column vector constructed from the incident wave k_0 . One can solve Eq. (38) using ordinary numerical libraries and thus obtain the scattering-state wave function of the given incident wave. We solve Eq. (38) for each incident wave from each probe and calculate the electron density and the current, as described in the following subsections. The computing time to solve Eq. (38) increases as the

third power of the number of orbitals (N_{tot}) when an ordinary numerical algorithm for a dense matrix is used. In the case of a very large system, it is very likely for the matrices \mathcal{A} and \mathcal{B} of Eq. (38) to be sparse ones, so the computing time can be decreased greatly with algorithms exploiting the sparsity of the matrices.

H. Nonequilibrium electron density

The system of interest is an open system with scattering states and bound states. Since the scattering states have a continuous energy spectrum, the calculation of the electron density requires an integration of wave functions of occupied scattering states. The occupation of the scattering states is governed by the two chemical potentials of the probes; that is, the scattering states incident from the first (second) probe are fully occupied up to its chemical potential μ_1 (μ_2). Thus, the electron density is

$$\begin{aligned} \rho(\mathbf{r}) = & 2 \int_{-\infty}^{\mu_1} dE \sum_{k, \mathbf{k}_{\parallel}} |\psi_{k, \mathbf{k}_{\parallel}}^{(1)}(\mathbf{r}, E)|^2 D_{k, \mathbf{k}_{\parallel}}^{(1)}(E) \\ & + 2 \int_{-\infty}^{\mu_2} dE \sum_{k, \mathbf{k}_{\parallel}} |\psi_{k, \mathbf{k}_{\parallel}}^{(2)}(\mathbf{r}, E)|^2 D_{k, \mathbf{k}_{\parallel}}^{(2)}(E) \\ & + 2 \sum_{E_b} |\psi_b(\mathbf{r}, E_b)|^2 f(E_b), \end{aligned} \quad (39)$$

where $\psi_{k, \mathbf{k}_{\parallel}}^{(l)}(\mathbf{r}, E)$ is the wave function of a scattering state (at energy E) incident from the l th probe with a wave number k perpendicular to the metal surfaces and a wave vector \mathbf{k}_{\parallel} parallel to the metal surfaces and $D_{k, \mathbf{k}_{\parallel}}^{(l)}(E)$ is the density of states per spin at the perpendicular wave number k and the parallel wave vector \mathbf{k}_{\parallel} in the l th probe far away from the resistive region. The third term in Eq. (39) is the contribution of occupied bound states, if they exist, with $\psi_b(\mathbf{r}, E_b)$ as wave functions of bound states, E_b as the corresponding energies, and $f(E_b)$ as the corresponding occupation numbers per spin. The scattering states $\psi_{k, \mathbf{k}_{\parallel}}^{(l)}(\mathbf{r}, E)$ are normalized by normalizing their incident-wave components in a unit cell in the l th probe. This normalization condition should be consistent with the unit of the density of states $D_{k, \mathbf{k}_{\parallel}}^{(l)}(E)$ so that they produce correct values of the electron density when the first term on the right-hand side in Eq. (39) is applied to a single probe.

In Eq. (39), we need the occupation numbers $f(E_b)$ of bound states if they exist in the resistive region. Obviously, a bound state is fully occupied (unoccupied) when its energy is lower (greater) than both of the two chemical potentials. However, if the energy of a bound state is between the two chemical potentials, its occupation number becomes undetermined within the present formalism although it would be determined in reality by a certain physical interaction or a specific initial condition. Furthermore, if a bound state of very long lifetime exists between the two chemical potentials, the electronic transport properties of the system will show quantum-dot behaviors with a Coulomb blockade, which is not within the scope of the present theory. Thus, in the present work, assuming hopefully that no true bound

state exists between the two chemical potentials, we count bound states up to the lower chemical potential only. Therefore, for the case $\mu_1 \geq \mu_2$, the electron density is given by

$$\rho(\mathbf{r}) = \rho(\mathbf{r}, \mu_2) + \int_{\mu_2}^{\mu_1} dE \sum_{k, \mathbf{k}_{\parallel}} |\psi_{k, \mathbf{k}_{\parallel}}^{(1)}(\mathbf{r}, E)|^2 D_{k, \mathbf{k}_{\parallel}}^{(1)}(E), \quad (40)$$

where $\rho(\mathbf{r}, \mu_2)$ is the electron density of all scattering and bound states whose energy is lower than μ_2 . Instead of finding scattering states and bound states to obtain the density $\rho(\mathbf{r}, \mu_2)$, we calculate the energy eigenstates ψ_c of a submatrix of the Kohn-Sham Hamiltonian matrix, which corresponds to a large cluster containing the resistive region, the intermediate regions, and several unit cells of the bulk regions, and then obtain the density $\rho(\mathbf{r}, \mu_2)$ using ψ_c :

$$\rho(\mathbf{r}, \mu_2) = 2 \sum_{E_i < \mu_2} |\psi_c(\mathbf{r}, E_i)|^2. \quad (41)$$

One can check the convergence of $\rho(\mathbf{r}, \mu_2)$ with respect to the size of the cluster.

The integral in Eq. (40) is then evaluated with the scattering-state wave functions obtained for a large number of energies $\{\epsilon_i\}$ between the two chemical potentials, i.e., for a given $(k, \mathbf{k}_{\parallel})$:

$$\int_{\mu_2}^{\mu_1} dE |\psi_k^{(1)}(\mathbf{r}, E)|^2 D_{k, \mathbf{k}_{\parallel}}^{(1)}(E) \approx \sum_i |\psi_k^{(1)}(\mathbf{r}, \epsilon_i)|^2 N_{k, \mathbf{k}_{\parallel}}^{(1)}(E_i, E_{i+1}) \quad (42)$$

where $E_i < \epsilon_i < E_{i+1}$ and $N_{k, \mathbf{k}_{\parallel}}^{(1)}(E_i, E_{i+1})$ is the number of states between E_i and E_{i+1} for the energy band of the wave number k ,

$$N_{k, \mathbf{k}_{\parallel}}^{(l)}(E_i, E_{i+1}) = \int_{E_i}^{E_{i+1}} dE D_{k, \mathbf{k}_{\parallel}}^{(l)}(E). \quad (43)$$

The accuracy of the integration depends on the set of energies where the scattering-state wave functions are obtained. When the shape of a scattering-state wave function changes rapidly in energy, one should make the energy grid dense. Scattering-state wave functions change rapidly especially when they are close to a resonance with a quasibound state. In such cases, matrix \mathcal{A} in Eq. (38) is close to a singular matrix and the amplitude of the scattering-state wave function becomes large. Thus, starting with a prespecified initial energy grid, we evaluate the amplitude of the obtained scattering-state wave functions and we introduce energy subgrids at the energies where the amplitude of any wave function is larger than a certain criterion. This is an *apparent* case for performing energy subgrids. However, if the initial energy grid is not close enough to a certain quasibound energy level, one will not observe the corresponding resonance. This is a *hidden* case that needs energy subgrids. To find all resonances including any hidden case, we consider the reciprocal of the condition of matrix \mathcal{A} in 1-norm,⁴³ $\text{rcond}(\mathcal{A})$, as a function of energy E . Since $\text{rcond}(\mathcal{A})$ is always positive and is zero if and only if the matrix \mathcal{A} is singular, all the resonances can be found by locating all the minima of $\text{rcond}(\mathcal{A})$ in a given energy range. To do this, we first evaluate

$\text{rcond}(\mathcal{A})$ at the initial energy grid and locate its minima at the grid. Then, introducing energy subgrids repeatedly near the minima, we refine their energy positions until all resonances are encountered for sure. By considering the amplitude of the scattering-state wave functions and by finding the minima of $\text{rcond}(\mathcal{A})$ of matrix \mathcal{A} of Eq. (38), one can generate a suitable energy grid for an accurate nonequilibrium electron density.

As mentioned in Sec. II C, the electron density obtained from the scattering states is used in the resistive region only. For this purpose, we construct the density matrix for the orbitals in the resistive and the intermediate regions only. This density matrix is sufficient to evaluate the electron density in the real-space grid in the resistive region.

I. Conductance and current

When a bias voltage V_b is applied, the difference in chemical potentials between the two probes is the same as the bias voltage,

$$V_b = (\mu_2 - \mu_1)/|e| \quad (44)$$

and the current is given by the integral,^{13–17}

$$I(V_b) = \frac{2|e|}{h} \int_{\mu_1}^{\mu_2} \langle T(E, \mathbf{k}_{\parallel}, V_b) \rangle dE. \quad (45)$$

Here, $T(E, \mathbf{k}_{\parallel}, V_b)$ is the sum of transmission probabilities of all conduction channels at parallel wave vector \mathbf{k}_{\parallel} and energy E , and $\langle \cdots \rangle$ represents average over \mathbf{k}_{\parallel} . The transmission probabilities depend on the applied bias voltage, resulting in a non-Ohmic electrical behavior, in general. Equation (45) reduces to the Landauer formula if the bias voltage is infinitesimally small. In the limit $V_b \rightarrow 0$, the current given by the integral is

$$\begin{aligned} I(V_b) &= \frac{2|e|}{h} \langle T(E_F, \mathbf{k}_{\parallel}, V_b = 0) \rangle (\mu_2 - \mu_1) + O(V_b)^2 \\ &= \frac{2e^2}{h} \langle T(E_F, \mathbf{k}_{\parallel}, 0) \rangle V_b + O(V_b)^2, \end{aligned} \quad (46)$$

where we used the fact that both μ_1 and μ_2 approach the Fermi energy E_F in this limit. Hence, we have the linear-response conductance G ,

$$G = \frac{I}{V_b} = \frac{2e^2}{h} \langle T(E_F, \mathbf{k}_{\parallel}, 0) \rangle, \quad (47)$$

which corresponds to the Landauer formula.

III. APPLICATIONS

In this section, we will apply our scattering-state method to a defective carbon nanotube, a four-carbon atomic chain, and a benzene-dithiol molecule, and then compare the results with other published results. In the following results, the small parameter h_{cut} for isolating the singularity in Eq. (10) is typically of the order of 10^{-10} eV, and it makes the complex band calculations successfully stable.

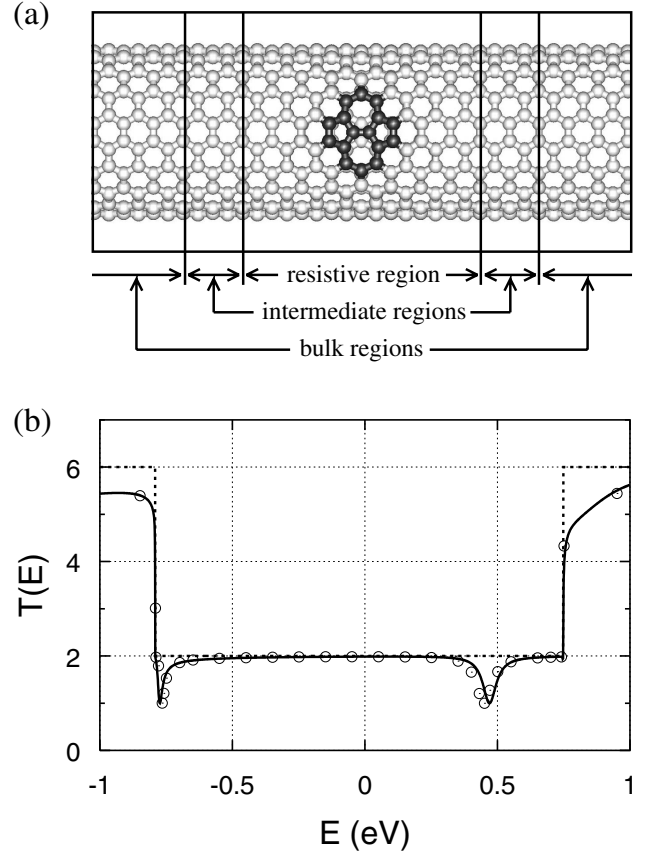


FIG. 2. (10,10) carbon nanotube with pentagon-heptagon-pair defect. (a) Atomic structure. (b) Transmission spectra. The solid line is the result of our present work using a double-zeta-polarization basis set to expand the electronic wave functions. An energy-grid spacing of 1 meV is used for the calculation of the spectrum and the Fermi energy is set to zero. Empty dots denote the result of the plane-wave-basis calculation (Refs. 27 and 28), plotted for comparison. The dashed line is the transmission spectrum without the defect.

A. Carbon nanotube with defect

The electrical conductance of carbon nanotubes with defects has been well studied with a first-principles plane-wave-basis method.^{27,28} In this subsection, we consider a (10,10) carbon nanotube with a pentagon-heptagon-pair defect and compare the result with that of the plane-wave-basis method. We focus on the transmission spectrum at zero bias voltage only since the voltage drop can hardly occur along metallic nanotubes.

Figure 2(a) shows the atomic geometry of a (10,10) carbon nanotube with a pentagon-heptagon-pair defect in it. For a detailed quantitative comparison of the results, we use the same atomic geometry as that used in Ref. 27, which is obtained by tight-binding molecular dynamics.⁴⁴ We employ an *ab initio* nonlocal pseudopotential for the carbon atom and a basis of linear combinations of pseudoatomic orbitals for the electron wave functions. We use a double-zeta-polarization (DZP) basis set, which has 13 pseudoatomic orbitals for each carbon atom. Only $\mathbf{k}_{\parallel}=0$ is used since the system is one dimensional.

We calculate the self-consistent Kohn-Sham potential along the defective carbon nanotube in two steps. In the first step, we calculate the self-consistent Kohn-Sham potential for a *perfect* (10,10) carbon nanotube. In this self-consistent calculation, the unit cell consists of 80 carbon atoms, which is twice the primitive unit cell of the tube, and a periodic boundary condition is imposed along the tubular axis. The unit cell is chosen so that the unit cell length is longer than the extent of the pseudoatomic orbitals of the carbon atoms. In the second step, we solve the Kohn-Sham equation self-consistently for the whole system which consists of the resistive region, the two intermediate regions, and the two semi-infinite bulk regions, as shown in Fig. 2(a). The resistive region is 19.6 Å long, with 340 carbon atoms and 4420 orbitals, and each intermediate is 4.9 Å long, with 80 atoms and 1040 orbitals. Thus, the total number (N_{tot}) of orbitals in the resistive region and the two intermediate regions is 6500, which is equal to the total number equations in Eqs. (37a)–(37c). The number of the complex bands in the bulk region is about 2×800 , significantly smaller than 2×1040 , after the null subspaces in \mathcal{H}_{ij}^+ and \mathcal{H}_{ij}^- are isolated by the use of h_{cut} . Since there is no applied bias voltage ($\mu_1 = \mu_2$), we can use the electronic wave functions of a cluster to obtain the charge distribution in the resistive region [Eqs. (40) and (41)]. A cluster of 820 carbon atoms is used in this work. During the self-consistent iteration, the electron distribution and the Kohn-Sham effective potential are updated within the resistive region only.

Figure 2(b) shows the transmission spectrum (or, equivalently, the linear-response conductance as a function of electron energy) at zero bias voltage in the (10,10) carbon nanotube with a pentagon-heptagon-pair defect. With the Fermi energy set to zero, the onset energies of the lower and upper subbands are at -0.79 and 0.75 eV, respectively. The transmission spectrum shows two dips at -0.77 and 0.47 eV due to resonant backscattering of conduction electrons by the quasibound states of the defect. Since the onset energies of the subbands were calculated more precisely than the Fermi energy in Ref. 27, the onsets of the subbands, rather than the Fermi energies, of the two calculations are exactly matched in Fig. 2(b) by shifting the plane-wave-basis result of Ref. 27 by 20 meV toward higher energies. The result of the present work agrees well with the plane-wave-basis calculation.^{27,28}

B. Carbon atomic wire

We consider a four-carbon atomic chain placed between two aluminum bars. The atomic configuration of the system is shown in Fig. 3(a). The resistive region is set to be 24.0 Å long, with 40 atoms (4 C and 36 Al), and each intermediate region is 8.1 Å long, with 18 Al atoms. In order to make a comparison with published results, the atomic positions are taken from Ref. 35. Furthermore, we used a single-zeta (SZ) basis set in order to have the same accuracy of the published work, although we note that the band structure of the aluminum bar is very sensitive to the accuracy of the basis functions expanding the electronic wave functions. Thus, we have 160 orbitals in the resistive region and 72 orbitals in each intermediate region. The total number (N_{tot}) of equa-

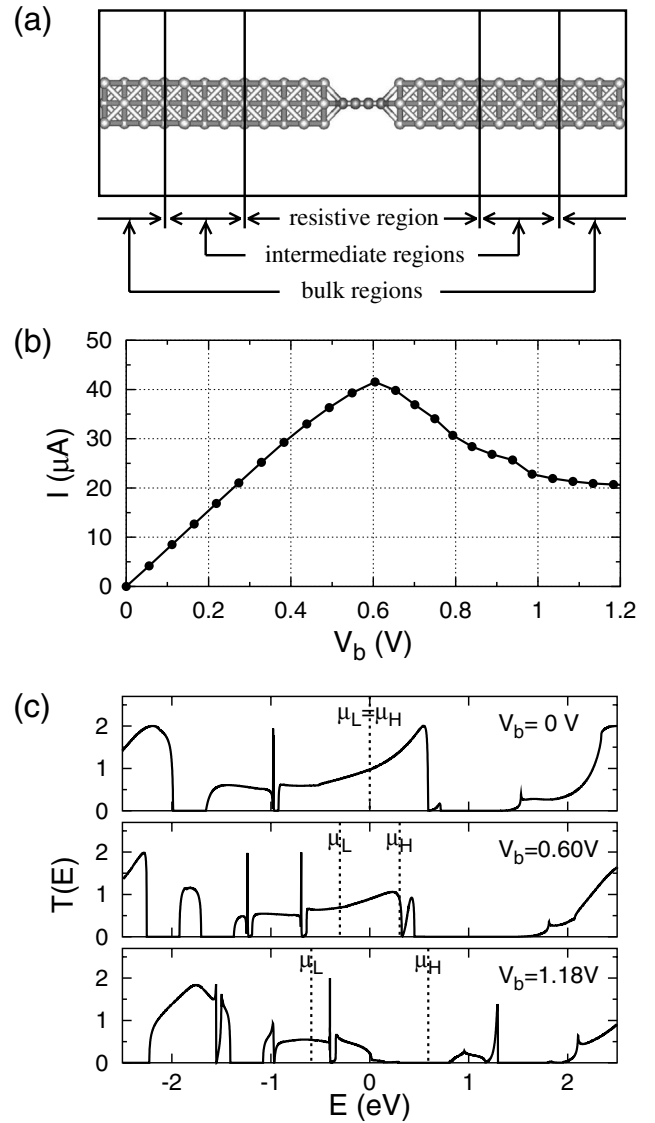


FIG. 3. Four-carbon-atomic chain between two aluminum bars. (a) Atomic structure. (b) Current-voltage characteristics. Filled dots denote obtained results and the solid line is a guide. Each dot requires a self-consistent calculation for electron redistribution and change in scattering states at the bias voltage. (c) Transmission spectra at the bias voltages of 0, 0.60, and 1.18 V.

tions in Eqs. (37a)–(37c) is 304. The number of the complex bands in the bulk region of the aluminum bars is about 2×60 , which is reduced from 2×72 by the isolation of the singularities in \mathcal{H}_{ij}^+ and \mathcal{H}_{ij}^- .

As in the case of the defective carbon nanotube in the previous subsection, we use only one k point ($\mathbf{k}_{\parallel} = 0$) and calculate the self-consistent electron distribution and the Kohn-Sham effective potential in two steps at each applied bias voltage. To obtain the nonequilibrium electron distribution at a finite bias voltage, the direct integration of the scattering-state wave functions in Eq. (40) is performed between the two chemical potentials with energy-grid points up to 2000. A cluster of 250 atoms is used to evaluate the charge density inside the resistive region below the lower chemical potential by Eq. (41).

Figure 3(b) shows the current-voltage characteristics obtained for the system. The result shows a peak in the current at a bias voltage of approximately 0.6 V and then shows a decrease of the current at larger bias voltage. The current-voltage curve looks very close to the previously published result.³⁵ Figure 3(c) shows the transmission spectra at three different bias voltages, which are obtained with an energy-grid spacing of 1 meV or less. As found in other publications, the transmission spectra depend very sensitively on the applied bias voltage.

C. Benzene-dithiol molecular junction

We calculated the current-voltage characteristics of a benzene-dithiol molecule contacted with two Au (111) surfaces. The atomic configuration is shown in Fig. 1. The two gold surfaces are separated by an atom-to-atom distance of 10.3 Å, and each surface has a rectangular surface area of 15.1×8.7 Å² within a supercell. The resistive region, which is chosen to be 24.5 Å long, consists of one benzene-dithiol (C₆H₄S₂) molecule and four Au layers on each side of the molecule, and each intermediate region, 7.1 Å long, has three Au layers. Since each Au layer has 18 atoms in the supercell, we have 264 atoms in the resistive and two intermediate regions. To expand the electronic wave functions, the SZ basis is used for Au *d* orbitals, the DZ basis for Au *s* orbitals, and the DZP basis for the atoms in the molecule. Thus, the resistive region has 1132 orbitals, and each intermediate region has 378 orbitals. The total number (N_{tot}) of orbitals in the resistive region and the two intermediate regions is 1888, which is the same as the number of equations in Eqs. (37a)–(37c). For each \mathbf{k}_{\parallel} , the number of the complex bands in the gold bulk region is about 2×270 , much smaller than 2×378 , after the singularities in \mathcal{H}_{ij}^{+} and \mathcal{H}_{ij}^{-} are isolated with h_{cur} .

In the self-consistent calculations for the electron density, we have used a 2×2 \mathbf{k}_{\parallel} grid in the two-dimensional Brillouin zone of \mathbf{k}_{\parallel} , with an energy-grid spacing of 5 meV (or less) for the scattering-state calculations between the two chemical potentials. The charge density below the lower chemical potential in Eq. (40) is obtained by Eq. (41) using a cluster of 373 atoms. For the transmission spectrum, \mathbf{k}_{\parallel} grids up to 8×8 are used with an energy-grid spacing of 10 meV.

Figure 4 shows the local part of the self-consistent Kohn-Sham effective potential with a finite bias voltage of $V_b = 2.0$ V [Fig. 4(a)], the difference of the self-consistent potentials for $V_b = 2.0$ V and $V_b = 0.0$ V [Fig. 4(b)], and the calculated current-voltage characteristics of the system [Fig. 4(c)]. The bias voltage of 2.0 V is applied to the system by lowering (raising) the Hartree potential of the left (right) probe by 1.0 V. We should note in Fig. 4(a) that the self-consistent potential is already close to the bulk values in the region $|z| > 5$ Å although the potential is matched at $z = \pm 12.3$ Å, which indicates that the self-consistent potential converges fast to the bulk values inside the gold probes. Figure 4(b) shows clearly that the voltage drop occurs mostly in the vacuum region and that the voltage drop is less steep along the molecule due to the molecule's polarizability. The conductance (I/V_{bias}) of the system is $0.38 G_0$ at an infinite

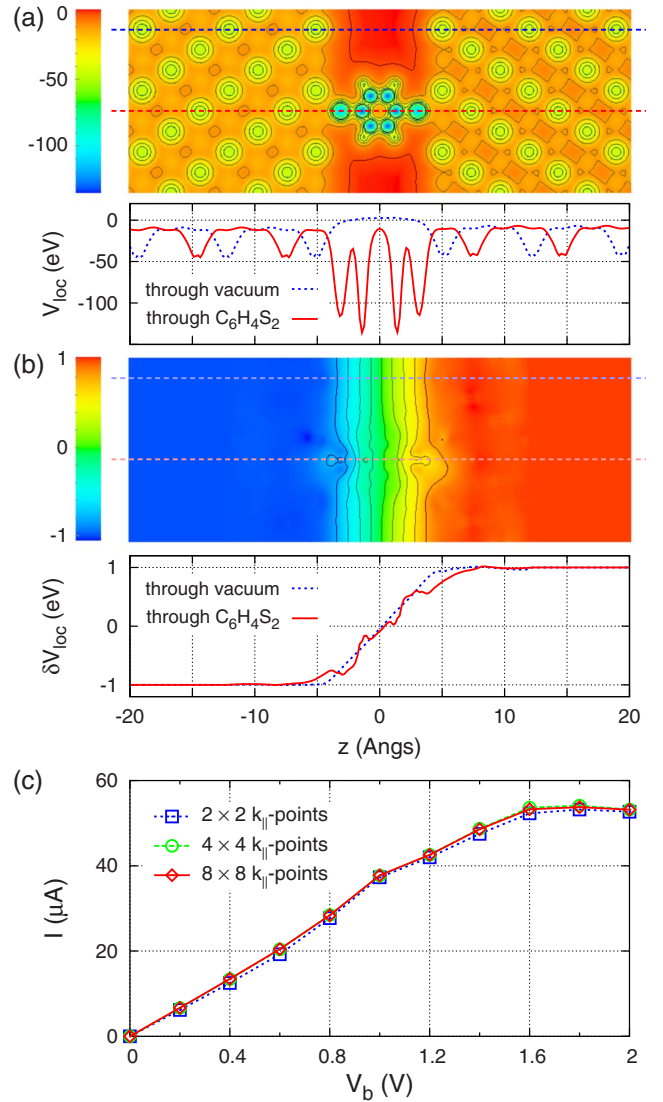


FIG. 4. (Color online) A benzene-dithiol molecule (C₆H₄S₂) contacted with gold probes. (a) Local part (V_{loc}) of the self-consistent Kohn-Sham effective potential when the bias voltage (V_b) is 2.0 V. In the upper panel, the potential is plotted in a color scale (in eV) on the plane containing the molecule, with dark solid contours for $V_{loc} = 0, -10, -20, \dots, -50$ eV. In the lower panel, the potential is plotted along the two dotted lines marked on the upper panel. (b) Local-potential difference, $\delta V_{loc} = V_{loc}(V_b = 2.0 \text{ V}) - V_{loc}(V_b = 0.0 \text{ V})$, plotted (in eV) at the same positions as in (a). Contours in the upper panel represent $\delta V_{loc} = -0.8, -0.6, -0.4, \dots, 0.8$ eV. (c) Current-voltage characteristics obtained with various \mathbf{k}_{\parallel} -grid points on the k_x - k_y plane.

tesimal bias voltage. The obtained current increases monotonically for the bias voltage ranging from 0 to 1.6 V. Then, the current is saturated up to 2.0 V. Results with different \mathbf{k}_{\parallel} grids show that the current is well converged with respect to the number of \mathbf{k}_{\parallel} -grid points.

Figure 5 shows the transmission spectra at $V_{bias} = 0.0, 1.0, 1.6$, and 2.0 V. At zero bias voltage, the transmission spectrum shows a high-transmission region from about -1.5 to 0.5 eV and a low-transmission region from about 0.5 to 2.5 eV. This feature implies that the high-transmission

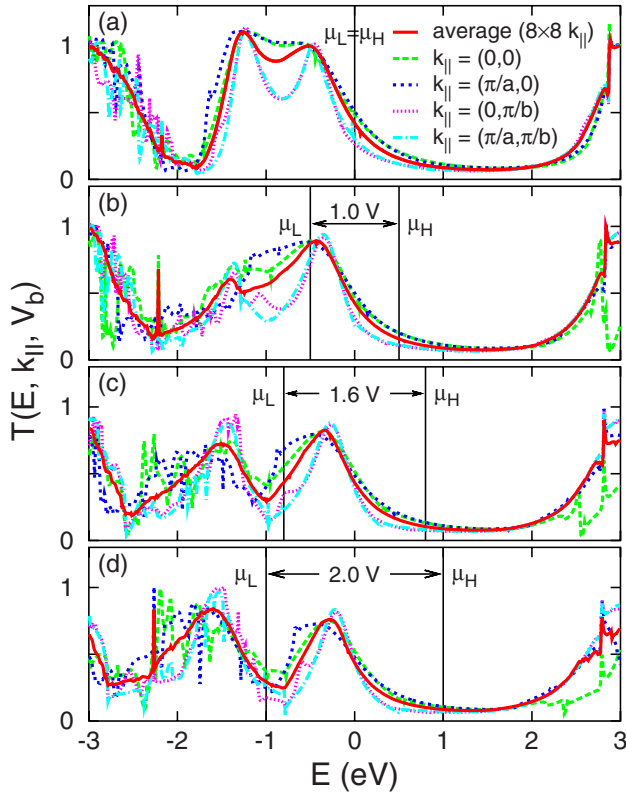


FIG. 5. (Color online) Transmission spectra through a benzene-dithiol molecule between two Au (111) surfaces at various bias voltages: (a) 0 V, (b) 1.0 V, (c) 1.6 V, and (d) 2.0 V. Each plot shows the transmission spectrum averaged over an 8×8 \mathbf{k}_{\parallel} grid and those for $\mathbf{k}_{\parallel} = (0,0)$, $(\frac{\pi}{a}, 0)$, $(0, \frac{\pi}{b})$, and $(\frac{\pi}{a}, \frac{\pi}{b})$, with $a = 15.1$ Å and $b = 8.7$ Å being the sizes of the supercell in the x and y directions, respectively. The molecule is placed on the xz plane.

region is due to the highest occupied molecular orbital (HOMO), which is substantially broadened in energy due to the coupling with the electrodes, and that the low-transmission region is due to the energy gap between the HOMO and the lowest unoccupied molecular orbital (LUMO). Since the HOMO is aligned only slightly below the Fermi level of the electrodes, significant conduction is allowed at the Fermi level.

Our results for the I - V characteristics and the transmission spectrum at zero bias voltage are in good agreement with the results of a previous calculation in which the gold electrodes are described atomistically.⁴⁵ However, our results disagree with the results of the jellium model in which the gold electrodes are represented by jellium.³⁸ The jellium model predicts an I - V curve which has a similar overall behavior to the experimental one, but the magnitude of the calculated current is 2 or 3 orders greater than the measured value.³⁸ In the experiment, the current is suppressed at a small bias voltage ranging from about -1 to 1 V, and then the current starts to increase significantly at a larger bias voltage.⁶ This behavior could be interpreted to mean that neither the HOMO nor the LUMO of the molecule is close to the Fermi level of the gold electrodes at zero bias voltage, implying that charge transfer between the molecule and the electrodes is negligible and

that the molecule has no net charge in the experiment. The present atomistic calculations and those in Ref. 45 also yielded a current that is orders of magnitude larger than experiment. Thus, a proper understanding of this particular experiment remains an open issue.

IV. SUMMARY

We have presented an *ab initio* scattering-state method for simulating nonlinear electrical transport in nanometer-scale samples, which is based on the first-principles density functional pseudopotential method and a localized-orbital expansion of the electronic wave function. In our method, we divide a two-probe setup of the conductance measurement into five regions: a resistive region, two intermediate regions, and two semi-infinite bulk regions. The electron density and the Hartree potential are calculated in an appropriate manner in different regions, and then they are combined to describe the whole system. One of the assumptions made is that the resistive region, which consists of the nanometer-scale sample and some parts of the probes connected to it, is large enough to contain all of the voltage drop so that the electron density and the Hartree potential profile in the intermediate and the bulk regions are virtually the same as their corresponding bulk values. In the self-consistent calculation at each finite bias voltage, the electron density in the resistive region is obtained from the scattering-state wave functions, and it determines the Hartree potential in the same region. When self-consistency is reached, the current through the sample is obtained by integrating the transmission of the scattering states. We have applied our method to a defective carbon nanotube, a carbon atomic wire, and a benzene-dithiol molecular junction. In these applications, we have obtained results which are consistent with those in the literature.

Our scattering-state method is a complementary approach to the NEGF method, providing stable and efficient algorithms to obtain the complex band structures, scattering-state wave functions, and the nonequilibrium electron density. Since the method deals with wave functions directly, it has the advantage that it is straightforward to analyze contributions of various electronic states to the total electrical current. The calculation of the complex bands is stabilized by isolating the singularity with a proper singular-value decomposition. The nonequilibrium electron density is then obtained accurately and efficiently by making energy grids dense enough only near the resonant energies of the scattering states.

Our method provides a basic framework to study the electronic structure and the electrical transport properties of open systems which are infinite with no periodic boundary conditions such as molecular junctions, surfaces, interfaces, and nanometer-scale quantum structures. It can be generalized straightforwardly for spin-dependent electronic transport within the local spin density approximation and can be applied to magnetic structures such as magnetic tunnel junctions as well.

ACKNOWLEDGMENTS

This work was supported by National Science Foundation Grant No. DMR04-39768, by the Office of Science, Office of Basic Energy Sciences, Division of Materials Sciences and Engineering Division, U.S. Department of Energy under Contract No. DE-AC02-05CH11231, by Yonsei University

Research Fund of 2005, and by the core capability enhancement program of KIST, “Massive Scientific Calculation Technology for Modelling of Nano Process and Devices.” Computational resources have been provided by the KISTI under the Seventh Strategic Supercomputing Support Program, NSF at the NPACI, and DOE at the NERSC.

*h.j.choi@yonsei.ac.kr

- ¹J. M. Krans, J. M. van Ruitenbeek, V. V. Fisun, I. K. Yanson, and L. J. de Jongh, *Nature* (London) **375**, 767 (1995).
- ²E. Scheer, N. Agraït, J. C. Cuevas, A. L. Yeyati, B. Ludoph, A. Martín-Rodero, G. R. Bollinger, J. M. van Ruitenbeek, and C. Urbina, *Nature* (London) **394**, 154 (1998).
- ³A. I. Yanson, G. R. Bollinger, H. E. van den Brom, N. Agraït, and J. M. van Ruitenbeek, *Nature* (London) **395**, 783 (1998).
- ⁴H. Mehrez, A. Wlasenko, B. Larade, J. Taylor, P. Grütter, and H. Guo, *Phys. Rev. B* **65**, 195419 (2002).
- ⁵R. H. M. Smit, C. Untiedt, G. Rubio-Bollinger, R. C. Segers, and J. M. van Ruitenbeek, *Phys. Rev. Lett.* **91**, 076805 (2003).
- ⁶M. A. Reed, C. Zhou, C. J. Muller, T. P. Burgin, and J. M. Tour, *Science* **278**, 252 (1997).
- ⁷H. Park, J. Park, A. K. L. Lim, E. H. Anderson, A. P. Alivisatos, and P. L. McEuen, *Nature* (London) **407**, 57 (2000).
- ⁸J. Park *et al.*, *Nature* (London) **417**, 722 (2002).
- ⁹W. Liang, M. P. Shores, M. Bockrath, J. R. Long, and H. Park, *Nature* (London) **417**, 725 (2002).
- ¹⁰A. M. Rawlett, T. J. Hopson, L. A. Nagahara, R. K. Tsui, G. K. Ramachandran, and S. M. Lindsay, *Appl. Phys. Lett.* **81**, 3043 (2002).
- ¹¹J. Reichert, H. B. Weber, M. Mayor, and H. v. Löhneysen, *Appl. Phys. Lett.* **82**, 4137 (2003).
- ¹²S. A. Getty, C. Engrakul, L. Wang, R. Liu, S.-H. Ke, H. U. Baranger, W. Yang, M. S. Fuhrer, and L. R. Sita, *Phys. Rev. B* **71**, 241401(R) (2005).
- ¹³R. Landauer, *IBM J. Res. Dev.* **1**, 223 (1957); **32**, 306 (1988).
- ¹⁴R. Landauer, *Philos. Mag.* **21**, 863 (1970).
- ¹⁵D. S. Fisher and P. A. Lee, *Phys. Rev. B* **23**, 6851 (1981).
- ¹⁶M. Büttiker, Y. Imry, R. Landauer, and S. Pinhas, *Phys. Rev. B* **31**, 6207 (1985).
- ¹⁷M. Büttiker, *Phys. Rev. Lett.* **57**, 1761 (1986).
- ¹⁸M. L. Cohen, *Phys. Scr.* **T1**, 5 (1982).
- ¹⁹N. Troullier and J. L. Martins, *Phys. Rev. B* **43**, 1993 (1991).
- ²⁰L. Kleinman and D. M. Bylander, *Phys. Rev. Lett.* **48**, 1425 (1982).
- ²¹J. Ihm, A. Zunger, and M. L. Cohen, *J. Phys. C* **12**, 4409 (1979).
- ²²D. Sánchez-Portal, P. Ordejón, E. Artacho, and J. M. Soler, *Int. J. Quantum Chem.* **65**, 453 (1997).
- ²³N. D. Lang, *Phys. Rev. B* **52**, 5335 (1995).
- ²⁴N. D. Lang, *Phys. Rev. Lett.* **79**, 1357 (1997).
- ²⁵N. D. Lang and Ph. Avouris, *Phys. Rev. Lett.* **81**, 3515 (1998).
- ²⁶J.-L. Mozos, C. C. Wan, G. Taraschi, J. Wang, and H. Guo, *Phys. Rev. B* **56**, R4351 (1997).
- ²⁷H. J. Choi and J. Ihm, *Phys. Rev. B* **59**, 2267 (1999).
- ²⁸H. J. Choi, J. Ihm, S. G. Louie, and M. L. Cohen, *Phys. Rev. Lett.* **84**, 2917 (2000).
- ²⁹M. S. Fuhrer, *et al.* *Science* **288**, 494 (2000).
- ³⁰Y.-G. Yoon, M. S. C. Mazzoni, H. J. Choi, J. Ihm, and S. G. Louie, *Phys. Rev. Lett.* **86**, 688 (2001).
- ³¹Y.-G. Yoon, H. J. Choi, M. S. C. Mazzoni, and S. G. Louie (unpublished).
- ³²M. B. Nardelli, J.-L. Fattebert, and J. Bernholc, *Phys. Rev. B* **64**, 245423 (2001).
- ³³A. Calzolari, N. Marzari, I. Souza, and M. B. Nardelli, *Phys. Rev. B* **69**, 035108 (2004).
- ³⁴J. Taylor, H. Guo, and J. Wang, *Phys. Rev. B* **63**, 245407 (2001).
- ³⁵B. Larade, J. Taylor, H. Mehrez, and H. Guo, *Phys. Rev. B* **64**, 075420 (2001).
- ³⁶M. Brandbyge, J.-L. Mozos, P. Ordejón, J. Taylor, and K. Stokbro, *Phys. Rev. B* **65**, 165401 (2002).
- ³⁷S. V. Faleev, F. Leonard, D. A. Stewart, and M. van Schilfgaarde, *Phys. Rev. B* **71**, 195422 (2005).
- ³⁸M. Di Ventra, S. T. Pantelides, and N. D. Lang, *Phys. Rev. Lett.* **84**, 979 (2000).
- ³⁹The compensating charge is placed uniformly on a plane which is substantially away from the boundaries of the resistive region since the Hartree potential, when obtained by the Fourier transformation with a finite number of plane waves, will have a numerical error oscillating at the vicinity of the plane.
- ⁴⁰S. Sanvito, C. J. Lambert, J. H. Jefferson, and A. M. Bratkovsky, *Phys. Rev. B* **59**, 11936 (1999).
- ⁴¹J. K. Tomfohr and O. F. Sankey, *Phys. Rev. B* **65**, 245105 (2002).
- ⁴²The same singular-value decomposition is used in Ref. 41 to handle the singularity. In their method, the eigenvalue equation for the complex bands is modified but its dimension remains unchanged. In our method, however, the decomposition leads to a decrease of the dimension of the eigenvalue equation by twice the dimension of the null subspace, as given by Eqs. (29)–(31), and the decrease of the dimension of the eigenvalue equation is essential in making numerical calculations stable, as discussed below Eq. (31).
- ⁴³The 1-norm $\|\mathcal{A}\|_1$ is defined as the maximal value of the sums $S_j = \sum_i |A_{ij}|$. Then, $\text{rcond}(\mathcal{A}) = (\|\mathcal{A}\|_1 \cdot \|\mathcal{A}^{-1}\|_1)^{-1}$. See, for example, E. Anderson *et al.*, *LAPACK User's Guide*, 3rd ed. (SIAM, Philadelphia, 1999).
- ⁴⁴C. H. Xu, C. Z. Wang, C. T. Chan, and K. M. Ho, *J. Phys.: Condens. Matter* **4**, 6047 (1992).
- ⁴⁵K. Stokbro, J. Taylor, M. Brandbyge, J.-L. Mozos, and P. Ordejón, *Comput. Mater. Sci.* **27**, 151 (2003).